Accepted Manuscript

Title: Three dimesional numerical simulations of water droplet dynamics in a PEMFC gas channel

Authors: Xun Zhu, P.C. Sui, Ned Djilali

PII: S0378-7753(08)00498-9
DOI: doi:10.1016/j.jpowsour.2008.03.005
Reference: POWER 10506

To appear in: *Journal of Power Sources*

Received date: 5-2-2008
Revised date: 29-2-2008
Accepted date: 3-3-2008

Please cite this article as: X. Zhu, P.C. Sui, N. Djilali, Three dimesional numerical simulations of water droplet dynamics in a PEMFC gas channel, *Journal of Power Sources* (2007), doi:10.1016/j.jpowsour.2008.03.005

Manuscript submitted to *J. Power Sources-Feb. 4, 2008*

THREE DIMESIONAL NUMERICAL SIMULATIONS OF WATER DROPLET DYNAMICS IN A PEMFC GAS CHANNEL

Xun Zhu[1], P. C. Sui[2], Ned Djilali[2,*]
[1] Institute of Engineering Thermophysics, Chongqing University, Chongqing, China, 400044
[2] Institute for Integrated Energy Systems and Department of Mechanical Engineering, University of Victoria, Victoria, BC V8W 3P6, Canada

ABSTRACT

The dynamic behavior of liquid water emerging from the gas diffusion layer (GDL) into the gas flow channel of a polymer electrolyte membrane fuel cell (PEMFC) is modeled by considering a 1000 μm long air flow microchannel with a 250×250 μm^2 square cross section and having a pore on the GDL surface through which water emerges with prescribed flow rates. The transient three-dimensional two phase flow is solved using Computational Fluid Dynamics in conjunction with a volume of fluid method. Simulations of the processes of water droplet emergence, growth, deformation and detachment are performed to explicitly track the evolution of the liquid–gas interface, and to characterize the dynamics of a water droplet subjected to air flow in the bulk of the gas channel in terms of departure diameter, flow resistance coefficient, water saturation, and water coverage ratio. Parametric simulations including the effects air flow velocity, water injection velocity, and dimensions of the pore are performed with a particular focus on the effect of the hydrophobicity of the GDL surface while the static contact angles of the other channel walls are set to 45°. The wettability of the microchannel surface is shown to

* Corresponding author: ndjilali@uvic.ca

have a major impact on the dynamics of the water droplet, with a droplet splitting more readily and convecting rapidly on a hydrophobic surface, while for a hydrophilic surface there is a tendency for spreading and film flow formation. The hydrophilic side walls of the microchannel appear to provide some benefit by lifting the attached water from the GDL surface, thus freeing the GDL-flow channel interface for improved mass transfer of the reactant. Higher air inlet velocities are shown to reduce water coverage of the GDL surface. Lower water injection velocities as well as smaller pore sizes result in earlier departure of water droplets and lower water volume fraction in the microchannel.

Keywords: Water management; surface tension; hydrophobicity; porous media; gas diffusion layer; volume of fluid; computational fluid dynamics.

INTRODUCTION

Water management plays a critical role in the operation of PEMFCs. Water is often introduced into the cell through humidified reactants and is also produced in the cathode. The formation, phase change and transport of water have a major impact on the operation, performance and durability of PEM fuel cells [1,2]. Since in most plate-and-frame PEMFC designs liquid water shares the same flow passages with gas reactants, when liquid water is not removed from the cell at a sufficient rate transport of reactants is hindered and so-called flooding is results. Flooding due to water occurs over a wide range of length scale, i.e. in the meso-pores of the catalyst layer, micro-pores of the GDL and sub-mm gas channels. The mixed wetting properties of the surfaces forming the microchannels, combined with the small hydraulic diameters (~500μm), and low velocities (Reynolds numbers of order ~ 10^3 or less), result in two-phase flow regimes encountered in PEMFCs quite different from those in more classical engineering applications (e.g. [3,4]). The PEMFC flows are for the most part laminar and are characterized by larger ratios of surface to volume forces, with surface tension and viscous forces playing predominant roles. Key questions from the view point of fuel cell design are understanding of: the dynamics of liquid water droplets; the detachment process and the ensuing entrainment and interaction with the channel walls and other droplets; and the characterization of the pressure drop.

A number of techniques have been used in recent years to investigate two-phase flow in PEMFC gas channels, including visualization using transparent fuel cell hardware [5-10], neutron scattering imaging [11-14], IR-thermography [15], NMR [16], MRI [17] and fluorescence microscopy [18]. Custom designed fuel cell hardware with optical access allow

quite good resolution observations of droplet formation, flow regimes, droplet-droplet and droplet-wall interactions, and droplet size distribution. However the transparent windows used have different transport properties (thermal and electrical) and surface properties (roughness and wettability) from those of actual bipolar plate material, and hence care should be exercised in interpreting the observations. The uncertainties due to the use of different materials are circumvented with non-optical techniques, but most of these techniques have limited temporal and spatial resolution. Nevertheless, experimental insights obtained to date have been extremely valuable and clearly demonstrated that water blockage in the cathode flow channels reduces the effective electrochemical reaction area and results in mass transfer limitation.

Most modelling works on water transport in PEMFC have to date focused on the issues of water flow in the porous components of the cell, e.g. water in the form of saturation in porous media driven by capillary pressure [19-25] and water in the form of absorbed water in the ionomer phase [26-28]. The transport equations derived for these models assume that water appears as a homogeneous phase within the representative volume. Such an assumption does not extend to liquid water moving in the gas channel due to the presence of large liquid interfaces as a result of interactions between surface tension and the channel walls. Analyses focused on the stability and liquid water motion have been reported by Chen et al. [29], Jiao et al. [30] and Quan et al. [31]. These numerical studies considered water droplets to be either suspended in the channel or attached to the wall of channel, or a water film on the channel wall, without taking into account the process of emergence of liquid water from the GDL into the gas channel. Recently Theodorakakos et al. [32] reported on a thorough investigation on the dynamics of water droplets in a microchannel based on PEMFC combining experiments and

three-dimensional simulations based on the volume-of-fluid (VOF) methodology. In this work the process was initiated assuming the presence of spherical droplets on the surface but without accounting for the emergence process from a pore. The VOF method was also adopted by the present authors in prior two-dimensional simulations [33, 34]. A key aspect of that work was the explicit consideration of the flow in a GDL pore and the tracking of liquid water emergence into the GDL. It was found that accounting for the initial connection of a droplet to a pore yield significantly different dynamics as well as critical air velocity for droplet detachment that are significantly higher from cases when a droplet is assumed initially stagnant and sitting on the surface. While these simulations have provided some valuable qualitative insights, a complete representation of the dynamic processes requires three-dimensional simulations.

In the present work, we extend our previous VOF model [33] to three-dimensions to investigate the physical mechanism of a water droplet emerging from a GDL pore, and perform an analysis of the growth, deformation, detachment, motion, coalescence and film formation and the associated water coverage and friction factors as a function of operation parameters and surface parameters.

NUMERICAL MODEL AND VOF METHOD

The volume-of-fluid (VOF) method used in this study was initially developed in the 1980s [35], and has been adopted in a number direct numerical simulations of time-dependent flows with multiple, immiscible liquids. In VOF the position of the interface between the fluids of interest is determined by applying a surface-tracking technique to a fixed Eulerian mesh, which is advantageous over methods such as lattice Boltzmann method (LBM), e.g. [36], or

boundary integral method [37], because it can be readily integrated into existing computational fluid dynamics (CFD) frameworks. A volume fraction indicator is used to determine the location of the interfaces of different phases in all cells of the computational domain [35], and a surface reconstruction scheme is then utilized to determine the shape of the interface [38]. The VOF method also allows for modelling of surface force based on the continuum force approach, making it possible to capture surface tension effects.

Numerical Method

Unsteady, isothermal laminar flow conditions are assumed to prevail for both air flow and water droplet motion inside the microchannel, since the bulk flow Reynolds number is less 650 and the heat generation and heat transfer are negligible. The three-dimensional numerical model was implemented using the commercial CFD package, FLUENT 6.3.26, and the volume of fluid (VOF) method [39].

In the VOF technique, a single set of momentum equations is shared by both fluid phases, and the interface between phases is tracked for each computational cell throughout the domain by computing the volume fraction for the fluid k:

$$C_k(x,y,z,t) = \begin{cases} 0 & (\text{outside } k^{\text{th}} \text{ fluid}) \\ 1 & (\text{inside } k^{\text{th}} \text{ fluid}) \\ 0 \sim 1 & (\text{at the } k^{\text{th}} \text{ fluid interface}) \end{cases} \quad (1)$$

where C_k is the volume fraction function of k^{th} fluid. For all the fluids, the sum of the volume fraction function is equal to 1.

$$\sum_{k=1}^{n} C_k = 1 \quad (2)$$

The volume fraction function C_k is governed by the volume fraction equation [39] which is solved in every computational cell

$$\frac{\partial}{\partial t}(C_k \rho_k) + \nabla \cdot (C_k \rho_k \vec{u}_k) = 0 \tag{3}$$

Then, the two-phase fluid flows in the microchannel are modeled with the Navier-Stokes equation which is dependent on the volume fractions of all phases through the fluid properties ρ and μ.

$$\frac{\partial}{\partial t}(\rho \vec{u}) + \nabla \cdot (\rho \vec{u} \vec{u}) = -\nabla p + \nabla \cdot \left[\mu(\nabla \vec{u} + \nabla \vec{u}^{\mathrm{T}})\right] + \rho \vec{g} + \vec{F} \tag{4}$$

where p is the static pressure, $\vec{F}$ is a momentum source term related to surface tension, ρ and μ are the volume averaged density and dynamic viscosity. These are computed to account for the variable volume fractions for the two phase air-water system considered here:

$$\rho = \rho_1 + C_2(\rho_2 - \rho_1) \tag{5}$$

$$\mu = \mu_1 + C_2(\mu_2 - \mu_1) \tag{6}$$

where indices 1 and 2 represent air and water, respectively.

Surface tension is accounted for by using the continuum surface force (CSF) model [40], and is expressed in terms of the pressure jump across the interface, which depends on the surface tension coefficient, and is implemented in the momentum equation as a body force $\vec{F}$.

$$\Delta p = \sigma\left(\frac{1}{R_1} + \frac{1}{R_2}\right) \tag{7}$$

$$\vec{F}_{\mathrm{vol}} = \sigma \kappa_k \frac{\rho \nabla C_k}{\frac{1}{2}(\rho_1 + \rho_2)} \tag{8}$$

where ΔP is the pressure drop across the surface, σ the surface tension coefficient, R_1, R_2 are the surface curvatures as measured by two radii in orthogonal directions, The curvature κ_k is computed from local gradients in the surface normal at the interface,

$$\kappa_k = \nabla \cdot \left(\frac{n}{|n|}\right) \tag{9}$$

and the surface normal ***n*** is defined as the gradient of C_k, the volume fraction of the k^{th} phase.

$$n = \nabla C_k \tag{10}$$

Geometric Reconstruction

A piecewise linear interface calculation (PLIC) method [38] is used to geometrically reconstruct the free surface. In the PLIC method, the interface is approximated by a straight line of appropriate inclination in each cell having a volume fraction greater than zero or less than one. A key aspect of the PLIC technique is the accurate determination of the interface normal vector **n** which determines the slope of the interface line located such that it delimits a fluid volume matching the given volume fraction function for the cell. Once the interface is reconstructed, the fluid volume passing between adjacent cells in all directions of the computational domain can be calculated [39].

Simulation Domain and Mesh

Figure 1 shows a schematic illustration of the three-dimensional computational domain and the corresponding mesh. Base case conditions in this study correspond to a microchannel with 250×250 μm^2 square cross section and 1000 μm length with a pore of diameter D=50 μm on the GDL surface. These dimensions are representative of gas flow channels used in PEM fuel cells, and the pore size considered is typical of mean hydraulic diameter values observed in microscope images of gas-diffusion layers (GDL) [18]. Air flow enters the channel with a velocity U, and water enters the channel through the pore on the GDL surface with a velocity V. This scenario is an idealized representation simulating the emergence into the channel of water produced by the electrochemical reaction, and condensed and transported through the GDL. The fixed location of the GDL pore is consistent with experimental observation that indicates

water usually appears preferentially on certain sites of the GDL surface [41]. A structured orthogonal computational mesh with 62,835 cells is used for all cases. The grid dependency was tested by increasing and decreasing the number of grid nodes by 20 and 40% for the case of a GDL surface with a static contact angle 140°, and similar water droplet transport and deformation processes were obtained with all three grids. Preliminary simulations were performed with time step size of 10^{-6}, 10^{-7} and 10^{-8} sec., all yielding similar results, and all parametric simulations were consequently performed using a time step size of 10^{-7} sec. Therefore the resolution used in the simulation is considered appropriate.

Boundary and Initial Conditions

In the VOF simulations presented here the uniform velocity profiles are specified at channel air inlet and pore water inlet, cf. Fig. 1. A convective outflow condition is used at the microchannel outlet. The no-slip boundary condition is imposed along the walls of the microchannel. Surface tension and contact angle are specified on the wall as a boundary condition. The contact angles of all walls of the channel except the bottom wall (GDL) are set to 45° for all cases. The calculations are initiated with a uniform air velocity field initial field and no liquid water in the channel.

For the base case simulations, an air velocity of 10 m/s at a pressure of 1 bar and temperature of 298 K is used, with a corresponding Reynolds number for air flow Re_a, = 158, where the hydraulic diameter of the micro channel is employed as the characteristic length; this is of the same order of magnitude as flows encountered in automotive fuel cell stacks [27]. Water is injected at a velocity of 1 m/s and the corresponding Reynolds number for water

injection, Re_w, is 50 where the pore diameter is employed as the characteristic length; this is of the same order as velocities used in ex-situ fuel cell experiments and corresponds to operation under high current density and water production rates [41, 42]. The static contact angle of the bottom wall is set at 140°; this is based on the typical PTFE treatment used for carbon paper and carbon cloth GDLs to promote water transport.

RESULTS AND DISCUSSION

The dynamic motion and deformation of a blob of water emerging from a GDL pore into a gas channel in a PEM fuel cell are affected by factors including wettability of the walls, air velocity, water injection rate, and pore size. It can be expected that when a growing blob of water is subjected to a cross air stream, forces acting on it include shear stress, surface tension, pressure, gravity, and inertial force. The shape and motion of the droplet are determined by the combined effects of the forces. For a micro gas channel, surface tension will play a particularly important role in water droplet dynamics, and some of the pertinent dimensionless numbers that represent the ratio of surface tension to the other forces are the capillary number ($Ca = \frac{\mu u}{\sigma}$), Weber number ($We = \frac{\rho u^2 d}{\sigma}$), and Bond number ($Bo = \frac{\rho g d^2}{\sigma}$). For baseline conditions in this study, $Ca = 1.4\times10^{-2}$, $We = 0.7$ and $Bo = 3.4\times10^{-4}$ by using the water injection pore diameter D as the characteristic length as well as the density, viscosity, and surface tension coefficient of water. The relatively small values of *Ca* and *Bo* numbers indicate that surface tension is more influential than viscous force and gravitational force in the present simulation condition. Meanwhile, wettability of the wall, which is represented by the contact angle (θ), also is one of the key factors influencing droplet dynamics. On a flat surface, the contact angle defines

geometrically the angle formed by a liquid at the boundary where liquid, gas and solid intersect. A zero contact angle represents the completely hydrophilic case with total wetting and formation of liquid film on the surface, and conversely $\theta = 180^{o}$ represents a completely hydrophobic (non wetting) case.

In order to study the effects of these parameters on the dynamic behavior of a growing water droplet in the micro gas channel, a series of simulations with different static contact angle of the GDL surface, air velocity, water velocity, and GDL pore size are performed. In the following discussion, the computational results for each parametric simulation are shown first, followed by analysis on the observations of these simulations.

Effect of Static Contact Angle of GDL Surface

In a typical PEM Fuel Cell gas microchannel, a GDL consisting of teflonated carbon paper or carbon cloth forms one of the walls, while the other three walls are formed or machined into a bipolar plate made of treated carbon-based or metallic materials. The wettability of the GDL surface can be altered by varying the PTFE coating and has important impact on the dynamic behavior of a water droplet in the microchannel. This is because the force that holds the liquid water is the horizontal component of the surface tension on the triple-phase contact line, which is closely related to the static contact angle of the fluid on the surface. For the present study, investigation on the effects of surface wettability is performed with different static contact angle values of the GDL surface θ= 45°, 70°, 90°, 120°, 140°, 160°, 180°. Figures 2-5 show the selected results for the time revolution of the droplet for θ= 45°, 90°, 140°, 180°, respectively.

Figure 2 shows the time evolution of the droplet interface for θ=45°, which is hydrophilic GDL surface. Water emerges from the GDL pore into the gas channel to form a droplet spreading on the GDL surface from the beginning due to the surface hydrophilicity (t=0.2 ms). The air flow from the channel inlet hinders water from spreading upstream by the inertial force, while the water droplet spreads downstream and towards both the side walls of the microchannel at the same time. When the water droplet grows and spreads to reach the side walls (t=0.6 ms), it is dragged up to the side walls quickly by the surface tension on the triple-phase contact line (t=1.0 ms), then spreads on the hydrophilic side walls where the static contact angles are set as 45°. Meanwhile, a concave gas/liquid interface is formed at the corners of the side walls and the bottom wall, which induces a surface tension gradient between the center and the corner of the channel. This gradient drives the water from the center to the sides, and the liquid downstream GDL surface shrinks back based on the rule of mass conservation. A saddle shape interface is formed, and the GDL surface is covered by the liquid film. It is noted that a raised head of water droplet is formed at the location of pore all the time due to water enters continuously. Furthermore, the water film keeps growing and spreading downstream on the GDL surface and both the side walls with the constant injection water velocity and blocks part of the microchannel (t=2 ms). With the increasing water volume and surface, blocked microchannel induces increasing air flow velocity, hence increasing shear stress acts on the surface of the water film. This pushes the water film on the GDL surface and both the side walls to move downstream towards the channel outlet. During the process, the instability of the air flow and the increasing shear stress overcome the surface tension to induce the break away of the water film from the head of the incoming water (t=4 ms).

Figure 3 shows the deformation of water droplet for the case θ=90°. Compared to the highly hydrophilic GDL surface for θ=45°, the neutral wettability in this case allows the water droplet to grow higher with less spreading on the GDL surface. The surface tension dominates over other forces and keeps the shape of the water droplet fairly spherical. When the water droplet grows bigger gradually, the increasing shear stress due to the increasing air velocity through the blocked channel pushes the water droplet downstream. But the incoming water forms a head, and then a neck appears between the body and head of water droplet along with the motion of the water droplet (t=1 ms). Fast convection of the bulk of the water droplet downstream due to the greater shear force on the larger surface results in the formation of a narrow liquid trail held by surface tension (t=2 ms). As time progresses, the increasing size of the water droplet results in much larger shear stress and static pressure forces, inducing acceleration and higher velocities than in the trail, and detachment occurs eventually (t=2.5 ms). After detachment, the main body of the water droplet flows out of the channel outlet, and the water trail is dominated by surface tension and shrinks back to form a new water droplet at the front (t=3 ms). The time for the water droplet to reach the channel outlet is shorter in this case than for the highly hydrophilic case with θ=45°. It should also be noted that the quick motion of the water droplet is also due to the larger static contact angle of the GDL surface which results in smaller area of the solid/liquid interface for the same water volume as well as a shorter perimeter of the triple-phase contact line, and are thus subject to lesser resistance due to viscous and surface tension forces.

Figure 4 and 5 show the time evolution of dynamic behavior of water droplet for the cases of θ=140° and θ=180°, respectively, which have a hydrophobic GDL surface. Compared

with the hydrophilic cases, the emerging water droplet tends to grow much higher on the hydrophobic GDL surface, θ=140°, within the same growth time (t= 0.2 ms, 1 ms) hence the less area of solid/liquid interface as well as the shorter triple-phase contact line. Therefore the stronger shear and the pressure forces caused by the air flow around the water droplet dominate over surface tension and friction and induce faster downstream convection and removal of the water droplet. The incoming water from the pore has lower momentum and is unable to follow the motion of the bulk of the water droplet, thus a neck forms (t=1.3 ms). Consequently, detachment occurs earlier (t=1.4 ms) and the detached droplet is quickly convected out of the domain (t=1.6 ms). Comparing Fig. 5 where θ=180° with Fig. 4, the processes of deformation, detachment, and motion of the water droplet are faster. Furthermore, once the water droplet breaks away from the head of emerging water, it is gradually lifted from the GDL surface by the air flow and the suction (low static pressure) along its upper surface. There is correspondingly a gradual reduction of the triple-phase boundary line, and eventually the droplet lifts off completely from the GDL surface and is convected by the bulk air flow (t=1.5 ms). These simulations physically illustrate the impact of GDL wettability on the rates of water droplet formation, growth, detachment and convection, and the enhanced rates of removal of water droplets from a hydrophobic GDL surface.

The comparison of the three phase contact lines and the water coverage ratio, A_w, on GDL surface for equivalent water volume at different static contact angles is shown in Fig. 6. All the three phase contact lines spread downstream from the GDL pore, but it is clear that the water droplet on the hydrophobic surface has a shorter extended contact line and a greater droplet height. The water coverage ratio, defined as the ratio of water coverage area to GDL

surface, decreases with increasing static contact angle. Reduced water coverage of the GDL surface prevents blockage to oxygen pathways and is thus is operationally desirable in a fuel cell.

While droplet detachment occurs readily for a hydrophobic GDL, such detachment can also occur when hydrophobicity is reduced but only after longer periods of time and once the droplet diameter attains much larger critical sizes at which the air flow blockage is such that large pressure forces are exerted on the droplet. The dependence of the critical detachment diameter on contact angle is shown in Figure 7. Here the critical diameter or diameter of the water droplet at the time of detachment is defined by as the diameter of a sphere of the same volume as the detached fluid, and is plotted in non-dimensional form (normalized with the characteristic length of the microchannel). Fig. 7 shows the detachment diameter decreases with increasing hydrophobicity, but remains fairly constant once the static contact angle is greater than 140 degree. There are thus no benefits to increasing hydrophobicity beyond θ = 140°. A functional correlation between the detachment diameter and the static contact angle is also plotted in Fig.7 for the condition corresponding to air flow and water injection Reynolds numbers of 157 and 50, respectively.

An important parameter in fuel cell operation is the friction factor, or flow resistance coefficient, which determines the extent of flow maldistribution or non-uniformity induced in a manifold design due to partial flooding of one channel. The time evolution of the flow resistance coefficient, defined as

$$f = \Delta P \Big/ (\frac{1}{2}\rho u_a^2 \frac{L}{D_H}),$$

is shown in Fig. 8, where ΔP is the pressure drop between the inlet and outlet of the microchannel, u_a and ρ are the air inlet velocity and air density respectively, L and D_H are the length and hydraulic diameter of the micro channel respectively. The dimensionless time, τ, is normalized by the time when the detached water droplet just exits the channel, and f_a is the reference flow resistance coefficient for air only flow through the microchannel. For all the cases, the air flow resistance coefficient increases as time progresses due to increasing water volume blocking air flow, and drops back after the detached droplet moves out of the channel. The resistance coefficient is higher overall for the highly hydrophobic cases. This is because the highly hydrophobic surface results in taller water droplet that induce more severe blockage in the channel. To assess the additional pumping requirements compared due to the presence of liquid water, the resistance coefficient is normalized with and f_a, showing that liquid water can induce up to a threefold increase. As was the case for the detachment diameter, the flow resistance coefficients remain approximately the same when the static contact angle is greater than 140 degree.

The effect of the static contact angle of GDL surface on the coverage ratio and the water saturation, S_w, which is defined as a ratio of the water volume inside the microchannel to the volume of the microchannel, are shown in Figs. 9 and 10. Both water saturation and coverage ratio increase with time due to the continuous inflow of liquid water, and decrease with increasing static contact angle of the GDL surface resulting from the shorter detachment time and smaller detachment diameter of the water droplet on the higher hydrophobicity GDL. For the higher contact angles, the decrease in the coverage ratio occurs much earlier than the exit

time of the droplet and is associated with the droplet lift-off discussed earlier and illustrated in Fig. 5.

Simulations performed over longer integration times show that the flow patterns are quasi-periodic as shown in Fig. 11, with the time evolution of the flow resistance, water saturation and coverage ratio for the case θ=140°. Cycle to cycle variations occur due to the non-linear nature of the dynamic processes, but a clear recurring pattern of droplet formation, growth, detachment, and removal occurs is established.

Effect of Air Inlet Velocity

As is well established form operational practice, air flow rates in the gas channel has significant effect on water management on the direct impacts on water dynamics were investigated by varying air inlet velocity from 3 m/s to 15 m/s corresponding to the Reynolds number of air flow from 47 to 236. Compared with the baseline case for U=10 m/s (Re_a=157), cf. Fig. 4, the results for two selected cases are shown in Figs. 12 and 13 where the air inlet velocities are 5 m/s (Re_a=79) and 15 m/s (Re_a=236), respectively. Since the water injection velocity is maintained constant, these simulations can be interpreted as corresponding to an increase in stoichiometry. The results in Fig. 12 show that for a lower air inlet velocity, water droplets tend to grow larger with less deformation within the same period phase of injection time, e.g. t = 1.0 ms, due to weaker shear stress and pressure forces. This results in a longer three phase contact line and larger coverage area, and hence stronger surface tension enhancing the stability of the water droplet. The water droplet does eventually deform downstream (t=2.0 ms) when it grows large enough, and then a neck appears (t=2.5 ms). But the deformation rate is

slower compared to the baseline case in Fig. 4. The water droplet finally detaches (t=2.6 ms) and moves slowly to the channel outlet.

When the air inlet velocity is increased to 15 m/s, cf. Fig. 13, early and significant deformation occurs (t = 0.6 and 0.88 ms); the maximum height of the water droplet is reduced and detachment occurs as early a t=0.9 ms, with shedding of a droplet that is smaller than the baseline case, cf. Fig. 4. This is of course due to the relatively larger ratio of hydrodynamic to surface tension forces.

Figure 14 shows a comparison of three phase contact lines and water coverage ratio for equivalent water volumes for various air flow velocities. The downstream bias of the phase contact line is quite prominent at the higher air velocities, and water coverage ratio decreases with increasing air velocity consistent with operational observations at higher stoichiometry.

The detachment diameter of the water droplet and the flow resistance coefficient in the microchannel varying with the air inlet velocity are shown in Figs. 15 and 16. Both the detachment diameter and the flow resistance coefficient decrease with increasing air inlet velocity since the smaller detached water droplet associated with higher air velocity results in lower blockage, and hence reduced pressure drop. A functional correlation between the detachment diameter of the water droplet and the Reynolds number of air flow is included in Fig.15.

Effect of Water Injection Velocity

Water production varies in a PEM fuel cell depending on the load and operating conditions [43]. Most of the water generated in the cathode catalyst layer flows through the network of pores in the GDL and eventually enters the gas channel. The detailed mechanisms of

water transport at the GDL/gas channel interface are not entirely well understood and depend on several factors, including pore size, pore network in the GDL, phase change rates and capillary force in the GDL [18], but in any case there is a correlation between net liquid water flow rates and current density. A series of simulation was carried out for water injection velocities of V= 0.05 m/s, 0.1 m/s, 0.5 m/s, 1 m/s, and 2 m/s, corresponding to water flow Reynolds number ranging from 2.5 to 100. The flow patterns for two selected cases are shown in Figs. 17 and 18 respectively. Compared with the baseline case for V=1 m/s (Re_w=50) in Fig. 4, the lower water injection velocity shown in Fig. 17, V=0.1 m/s (Re_w=5), reveals similar dynamic behavior except a slower growth process and hence a longer time for detachment. However, the detachment time does not scale directly with the injection velocity and is not quite 10 times that of the baseline case, and the critical diameter for detachment is smaller. This is attributed to the relatively greater deformation of the droplet which is subjected to the air stream over a longer period during its slower growth phase.

When the water injection velocity is increased to 2 m/s (Re_w=100), on the other hand, a drastically different dynamic behavior is shown in Fig. 18. The faster water droplet growth rate is accompanied at the early stage, approx. t<0.8 ms, by an elongation and excursion of the water droplet towards the centre of the channel with relatively smaller coverage of the GDL surface than in the baseline case. The taller water droplet interacts with the air flow field in and significant deformation occurs at 0.8 ms with the water droplet being dragged by the fortified shear stress and pressure forces, and eventually re-attaching and covering the GDL surface at t=1.0 ms. The connecting “umbilical cord” connecting the droplet to the pore stretches and early detachment occurs at t=1.2 ms, with the larger detached droplet leaving behind a long

cord/wake of water connected to the pore. Subsequently this cord retracts partially to form a new droplet with a neck and wake, and a quasi-periodic growth and detachment pattern sets, but with the detachment location for the water droplet moving gradually downstream at every cycle and the cord of water becomes longer and longer which higher coverage of the GDL surface, and hence hindrance to oxygen transport.

Figure 19 shows the three phase contact lines for the same water volume at different water injection velocities, with the inset showing the water coverage ratio on the GDL surface. The three phase contact lines and the water coverage ratio show similar behaviour for a water injection velocity of less than 1 m/s, Re_w<50 but decreases drastically for higher water injection velocities.

The diameter of the water droplet at detachment, shown in Fig. 20, increases with Reynolds number as at higher water injection velocities more volume of water enters the microchannel at equivalent times thus forming bigger water droplets. Consequently, the flow resistance coefficient increases as well as shown in Fig. 21 due to the larger microchannel blockage. At low water injection velocities both the detachment diameter and the flow resistance coefficient are relatively insensitive to the injection rate. For the higher Reynolds number, the flow resistance coefficient increases first due to fast growth of the droplet then drops after the water droplet re-attaches to the GDL surface (see Fig. 18.d) thus reducing the blockage to air flow.

The effects of air inlet velocity and water injection velocity on water saturation and coverage ratio in the microchannel are shown in the Figs. 22 and 23, respectively. Both water saturation and coverage ratio decreases with increasing Reynolds number of air flow and

decreasing Reynolds number of water flow. Likewise, for higher Reynolds number of water flow, the coverage ratio remains small at the beginning due to the thinner and taller water droplet while it rises substantially after the water droplet is pushed down by the air flow to re-attach on the GDL surface.

Effect of pore size

The GDL structure is non-uniform and anisotropic and is characterized by a range of pore sizes. A simulation complementing the base case is presented here for a pore diameter of 25 μm (half of the baseline case). The water injection rate is half of the baseline case under the same injection velocity, and the resulting droplet flow pattern is presented in Fig. 24. Compared with the larger pore baseline case, the water droplet exhibits slower growth and deformation, and, due to the smaller water injection rate, induces smaller water coverage. However, for the equivalent water volume, the three phase contact line for the water droplet from the smaller pore deforms significantly further downstream than the baseline case as shown in Fig. 25. Thus for the smaller pore size, because of the weaker surface tension due to reduced connectivity with the GDL pore, shear and pressure forces overcome surface tension earlier and the droplet detaches at a smaller diameter.

CONCLUSIONS

Fundamental aspects of the dynamics a water droplet emerging from a pore into a gas microchannel were investigated using a three-dimensional CFD model in conjunction with the volume of fluid (VOF) method. The effects of the static contact angle of the bottom wall, air

inlet velocity, water injection velocity, and pore size on the water droplet dynamics were investigated. The main findings and conclusions are:

(1) The emergence of the water droplet into a micro gas channel is a highly dynamic and quasi-periodic process with cyclic formation, growth, deformation, detachment, and removal of water droplets.

(2) Wettability of the GDL surface has a strong impact on the emerging water droplet behavior. Hydrophobic walls result in earlier detachment of water droplets having smaller diameters, while hydrophilic walls results in spreading of the water droplet on the GDL surface. The frequency of the periodic process increases with decreasing wettability of GDL surface, and a high hydrophobicity surface promotes water removal. The detachment time, detachment diameter, water saturation, and coverage ratio decrease while the flow resistance coefficient increase with increasing static contact angle of the GDL surface.

(3) High air inlet velocity results in earlier deformation and detachment of the emerging water droplet with faster removal and smaller detachment diameter. The three phase contact line deforms further downstream significantly at higher air velocity. The water saturation, water coverage ratio, detachment diameter, and flow resistance coefficient decrease with increasing Reynolds number of air flow.

(4) High water injection velocities result in earlier detachment of the droplets with larger detachment diameter, and the detachment location moves gradually further downstream with every cycle, resulting in higher water coverage of the GDL surface. The detachment diameter, and flow resistance coefficient are found to be fairly insensitive to the injection rate at low water injection velocity.

(5) Water droplets emerging from a smaller pore exhibit slower growth and deformation, and result in smaller water coverage. For equivalent water volume, the three phase contact line deforms significantly further downstream inducing detachment at smaller droplet diameters.

ACKNOWLEDGEMENTS

XZ is grateful for the support by the National Natural and Science Foundation of China (No. 90410005), the Excellent Young Teachers Program of M0E , P. R. C. ([2003]355#), and the China Scholarship programs. ND acknowledges the financial support by the MITACS Network of Centres of Excellence, Ballard Power Systems and the Canada Research Chairs Program.

REFERENCES

1. J.J. Kowal, A. Turhan, K. Heller, J. Brenizer, M.M. Mench, J. Electrochem. Soc. **153** (2006), pp. A1971-A1978.
2. A. Taniguchi, T. Akita, K. Yasuda, Y. Miyazaki, J. Power Sources **130** (2004), pp. 42-49.
3. K.A. Triplett, S.M. Ghiaasiaan, S.I. Abdel-Khalik, D.L. Sadowski, Int. J. Multiphase Flow **25** (1999), pp. 377-394.
4. T.A. Trabold, Heat Transfer Engineering **26** (2005), pp. 3-12.
5. K. Tüber, D. Pocza, C. Hebling, J. Power Sources **124** (2003), pp. 403-414.
6. X.G. Yang, F.Y. Zhang, A.L. Lubawy, C.Y. Wang, Electrochem. and Solid State Letters **7** (2004), pp. A408-A411.
7. F.Y. Zhang, X.G. Yang, C.Y. Wang, J. Electrochem. Soc. **153** (2006), pp. A225-A232.
8. M.M. Mench, C.Y. Wang, M. Ishikawa, J. Electrochem. Soc. **150** (2003), pp. A1052-A1059.
9. K. Sugiura, M. Nakata, T. Yodo, Y. Nishiguchi, M. Yamauchi, Y. Itoh, J. Power Sources **145** (2005), pp. 526-533.
10. F.B. Weng, A. Su, C.Y. Hsu, C.Y. Lee, J. Power Sources **157** (2006), pp. 674-680.
11. R. Satija, D.L. Jacobson, M. Arif, S.A. Werner, J. Power Sources **129** (2004), pp. 238-245.
12. D. Kramer, J.B. Zhang, R. Shimoi, E. Lehmann, A. Wokaun, K. Shinohara, G.G. Scherer, Electrochimica Acta **50** (2005), pp. 2603-2614.
13. M.A. Hickner, N.P. Siegel, K.S. Chen, D.N. McBrayer, D.S. Hussey, D.L. Jacobson, M. Arif, J. Electrochem. Soc. **153** (2006), pp. A902-A908.
14. N. Pekula, K. Heller, P.A. Chuang, A. Turhan, M.M. Mench, J.S. Brenizer, K. Unlu, Nuclear Instruments & Methods in Physics Research Section a-Accelerators

Spectrometers Detectors and Associated Equipment **542** (2005), pp. 134-141.
15. A. Hakenjos, H. Muenter, U. Wittstadt, C. Hebling, J. Power Sources **131** (2004), pp. 213-216.
16. K.W. Feindel, L.P.A. LaRocque, D. Starke, S.H. Bergens, R.E. Wasylishen, J. Am. Chem. Soc. **126** (2004), pp. 11436-11437.
17. S. Tsushima, K. Teranishi, S. Hirai, Electrochem. and Solid State Letters **7** (2004), pp. A269-A272.
18. S. Litster, D. Sinton, N. Djilali, J. Power Sources **154** (2006), pp. 95-105.
19. Z.H. Wang, C.Y. Wang, K.S. Chen, J. Power Sources **94** (2001), pp. 40-50.
20. U. Pasaogullari, C.Y. Wang, J. Electrochem. Soc. **151** (2004), pp. A399-A406.
21. J.J. Baschuk, X.H. Li, J. Power Sources **86** (2000), pp. 181-196.
22. N.P. Siegel, M.W. Ellis, D.J. Nelson, M.R. von Spakovsky, J. Power Sources **128** (2004), pp. 173-184.
23. L.X. You, H.T. Liu, Int. J. Heat and Mass Transfer **45** (2002), pp. 2277-2287.
24. M.R. Hu, A.Z. Gu, M.H. Wang, X.J. Zhu, L.J. Yu, Energy Conversion and Management **45** (2004), pp. 1861-1882.
25. T. Berning, N. Djilali, J. Electrochem. Soc. **150** (2003), pp. A1589-A1598.
26. T.E. Springer, T.A. Zawodzinski, S. Gottesfeld, J. Electrochem. Soc. **138** (1991), pp. 2334-2342.
27. P.C. Sui, N. Djilali, ASME Journal of Fuel Cell Science and Technology **2** (2005), pp. 149-155.
28. J. Fimrite, H. Struchtrup, N. Djilali, J. Electrochem. Soc. **152** (2005), pp. A1804-A1814.
29. K.S. Chen, M.A. Hickner, D.R. Noble, Int. J. Energy Research **29** (2005), pp. 1113-1132.
30. K. Jiao, B. Zhou, P. Quan, J. Power Sources **157** (2006), pp. 226-243.
31. P. Quan, B. Zhou, A. Sobiesiak, Z.S. Liu, J. Power Sources **152** (2005), pp. 131-145.
32. A. Theodorakakos, T. Ous, A. Gavaises, J.M. Nouri, N. Nikolopoulos, H. Yanagihara, J. Colloid and Interface Science **300** (2006), pp. 673-687.
33. X. Zhu, P.C. Sui, N. Djilali, J. Power Sources **172** (2007), pp. 287-295.
34. X. Zhu, P.C. Sui, N. Djilali, Microfluidics and Nanofluidics **in press** (2008),
35. C.W. Hirt, B.D. Nichols, J. Comp. Phys. **39** (1981), pp. 201-225.
36. A. Golpaygan, N. Ashgriz. 14th Annual conference of the computational fluid dynamics of Canada (2006), Kingston, Canada.
37. J. Billingham, A.C. King, J. Fluid Mechanics **296** (1995), pp. 325-351.
38. D.L. Youngs (1982). Time-dependent multi-material flow with large fluid distortion. New York, Academic Press.
39. Fluent (2006). Fluent 6.2 User's Guide.
40. J.U. Brackbill, D.B. Kothe, C. Zemach, J. Comp. Phys. **100** (1992), pp. 335-354.
41. A. Bazylak, D. Sinton, Z.S. Liu, N. Djilali, J. Power Sources **163** (2007), pp. 784-792.
42. E.C. Kumbur, K.V. Sharp, M.M. Mench, J. Power Sources **161** (2006), pp. 333-345.
43. T. Berning, N. Djilali, J. Power Sources **124** (2003), pp. 440-452.

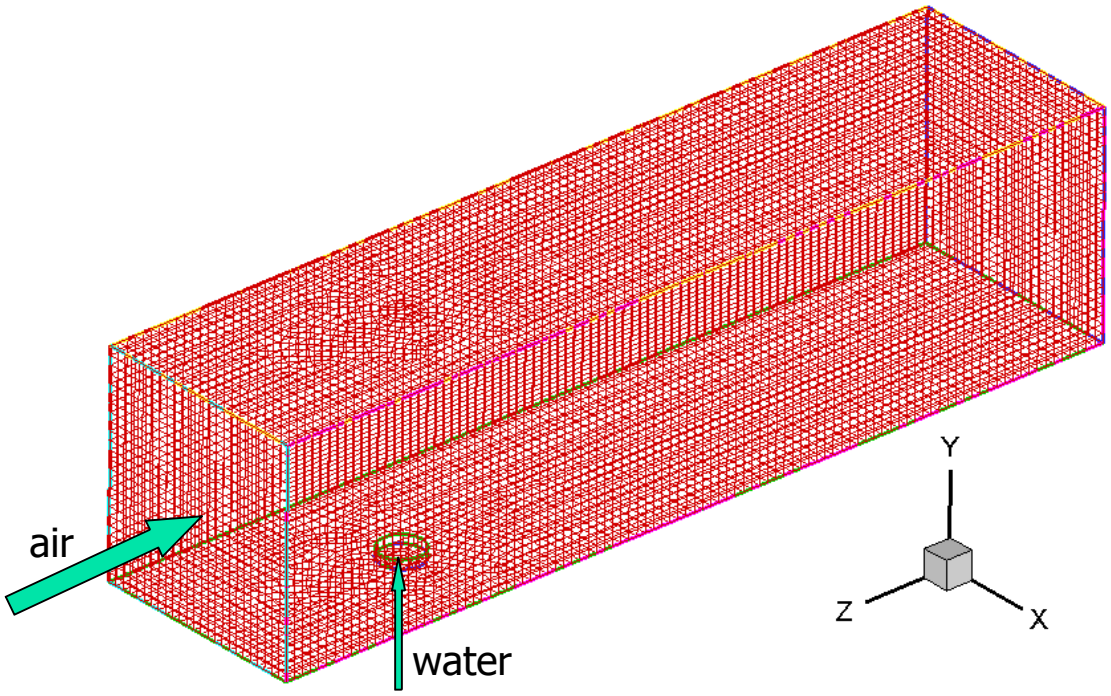

Figure 1 Computation domain and mesh for the three dimensional simulations

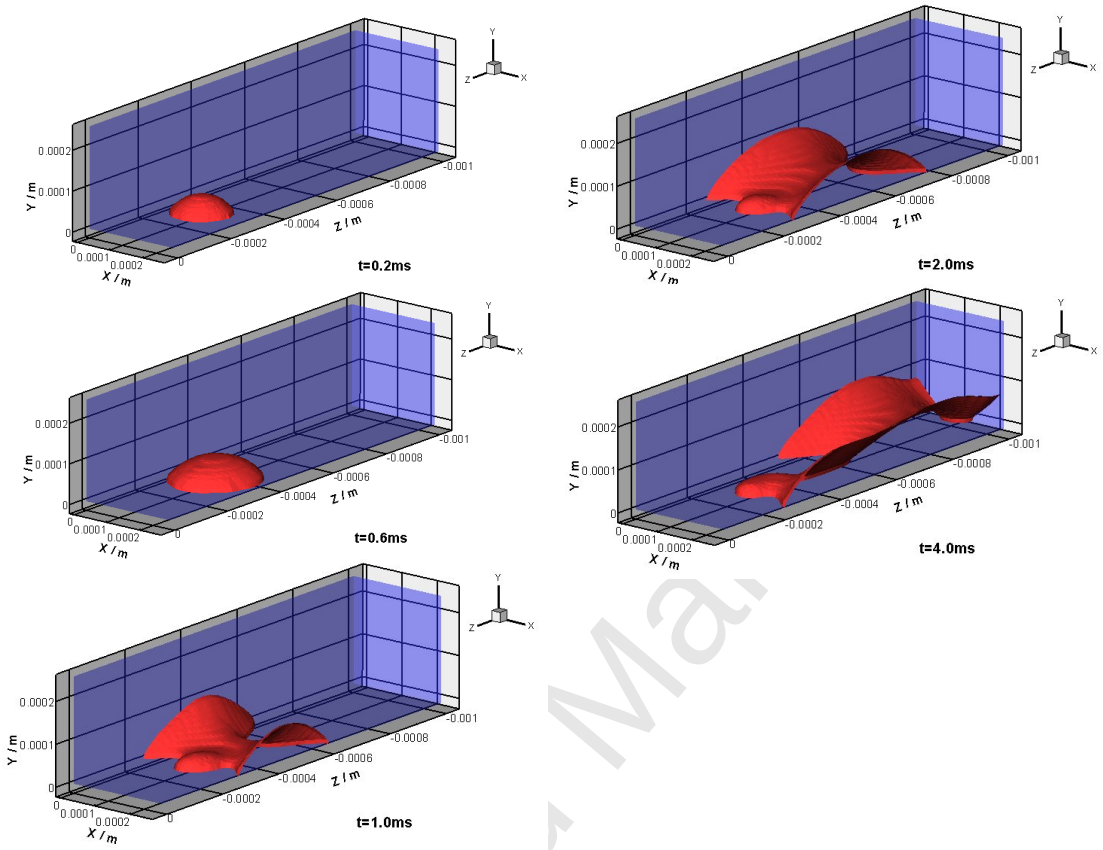

Figure 2 Time evolution of the emerging water droplet into the microchannel for θ=45°

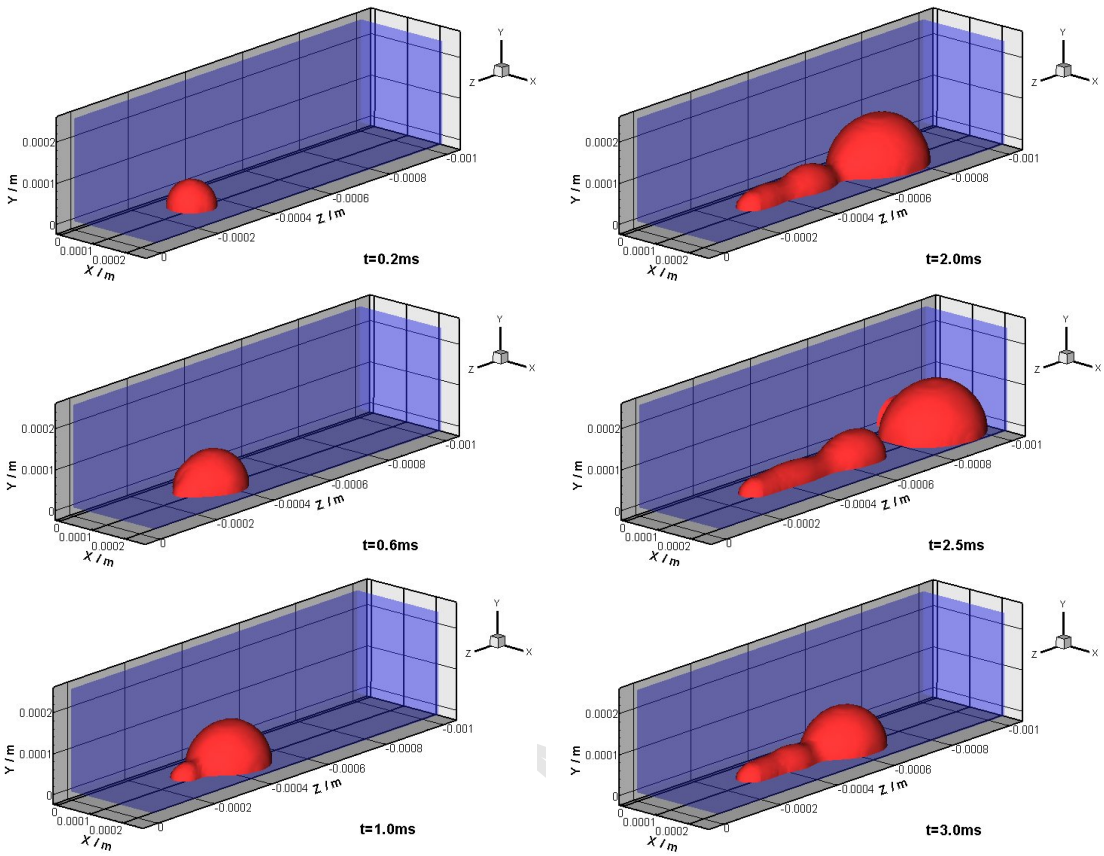

Figure 3 Time evolution of the emerging water droplet into the microchannel for θ=90°

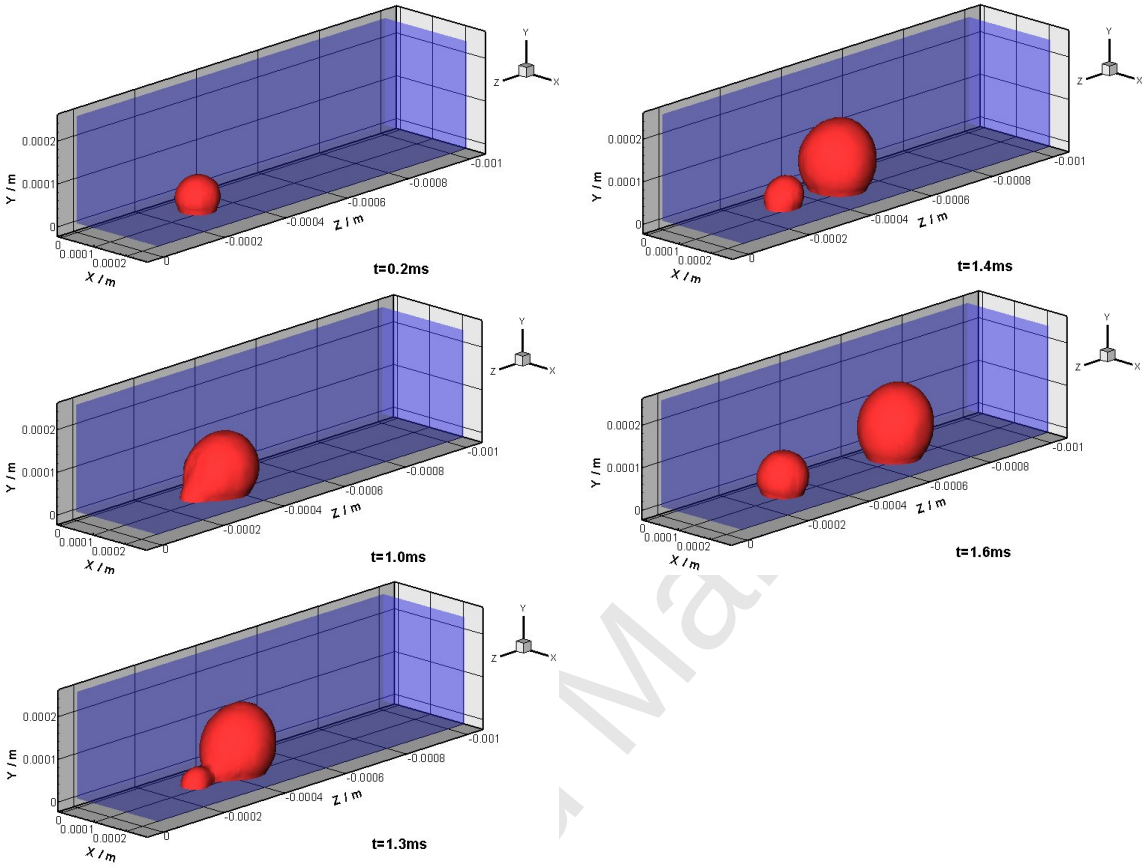

Figure 4 Time evolution of the emerging water droplet into the microchannel for θ=140°

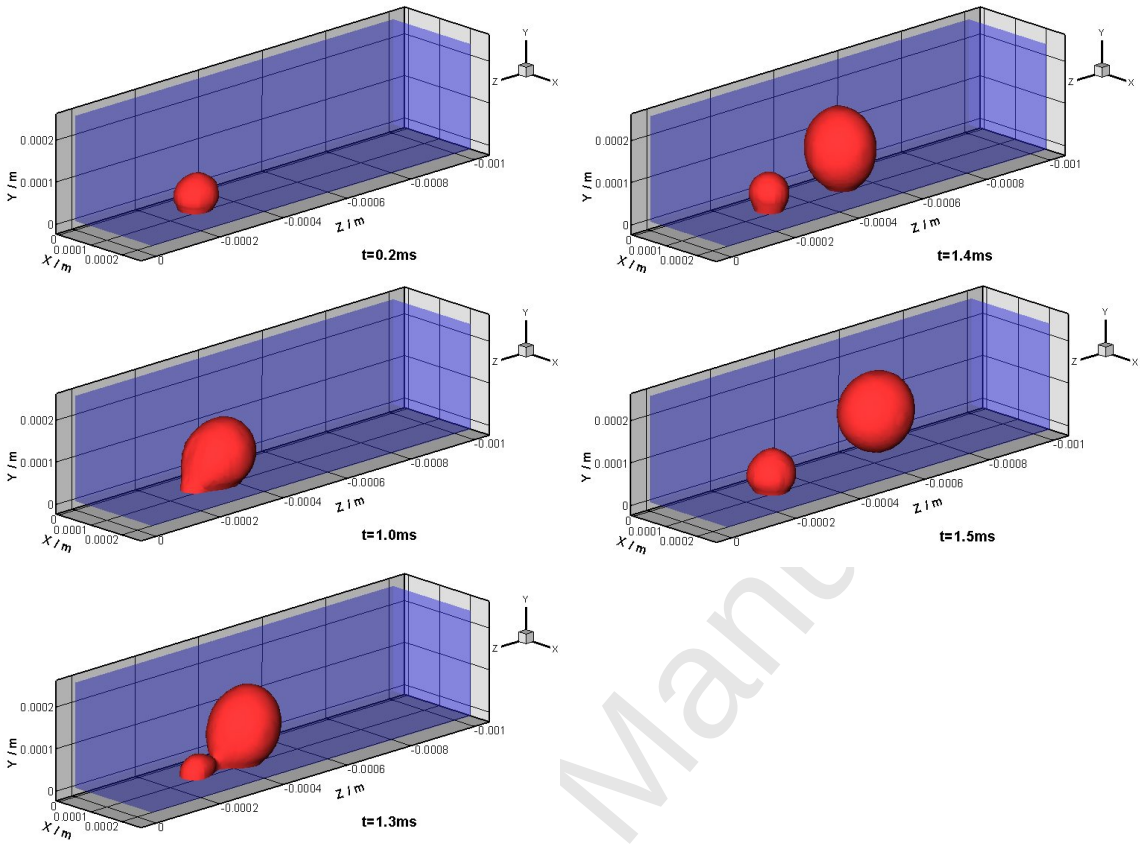

Figure 5 Time evolution of the emerging water droplet into the microchannel with θ=180°

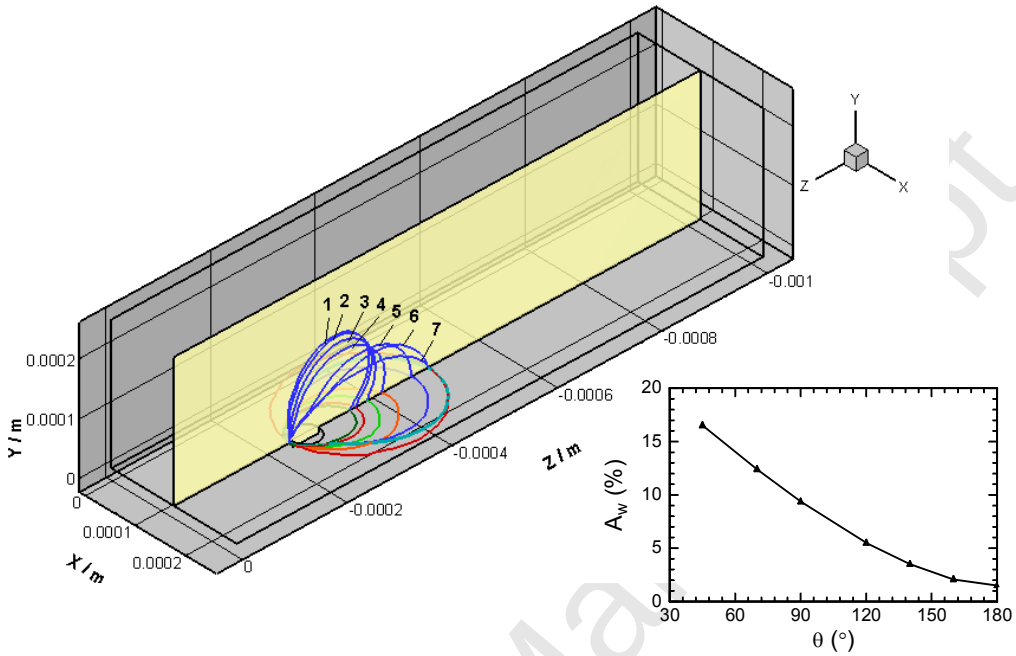

Figure 6 Three phase contact lines and coverage ratio for equivalent water volume at different static contact angle: 1-θ=180°, 2-θ=160°, 3-θ=140°, 4-θ=120°, 5-θ=90°, 6-θ=70°, 7-θ=45°

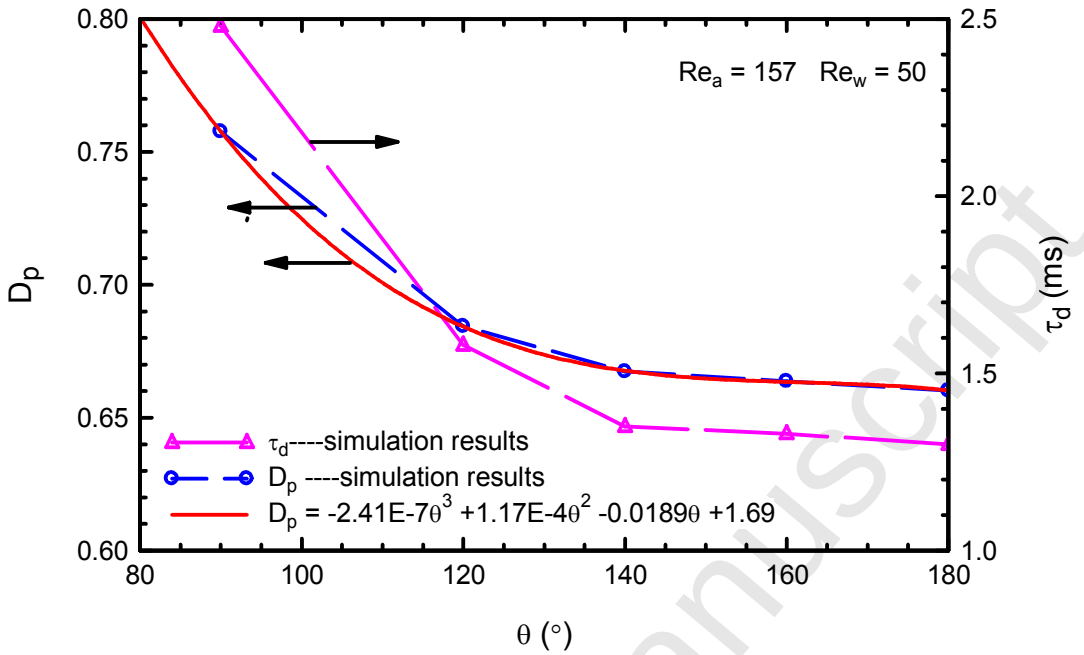

Figure 7 Detachment diameter of the water droplet varies with the static contact angle

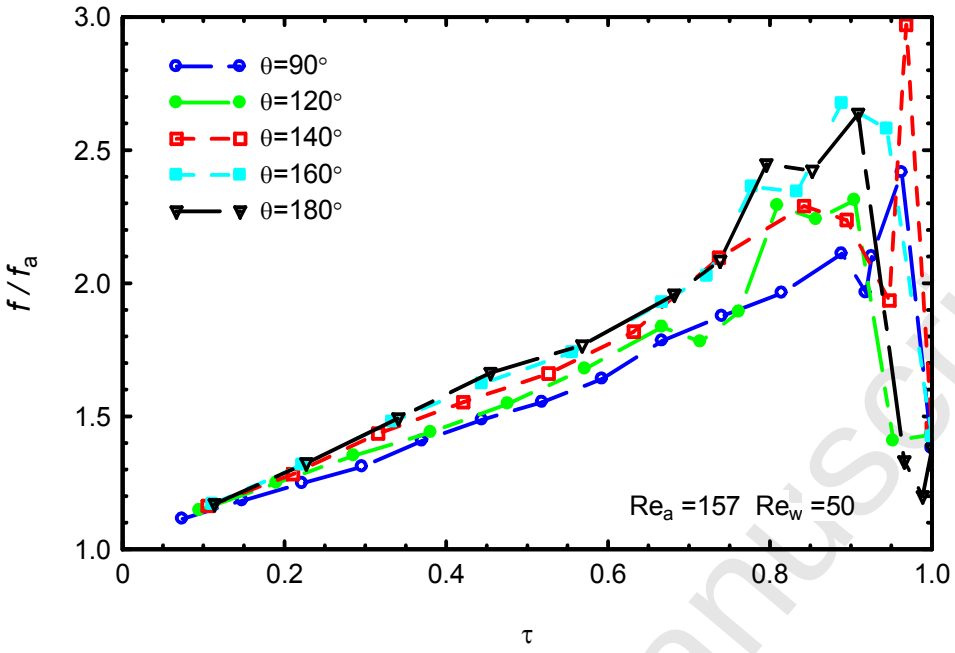

Figure 8 Effect of static contact angle of GDL surface on the relative flow resistance coefficient of the air flow

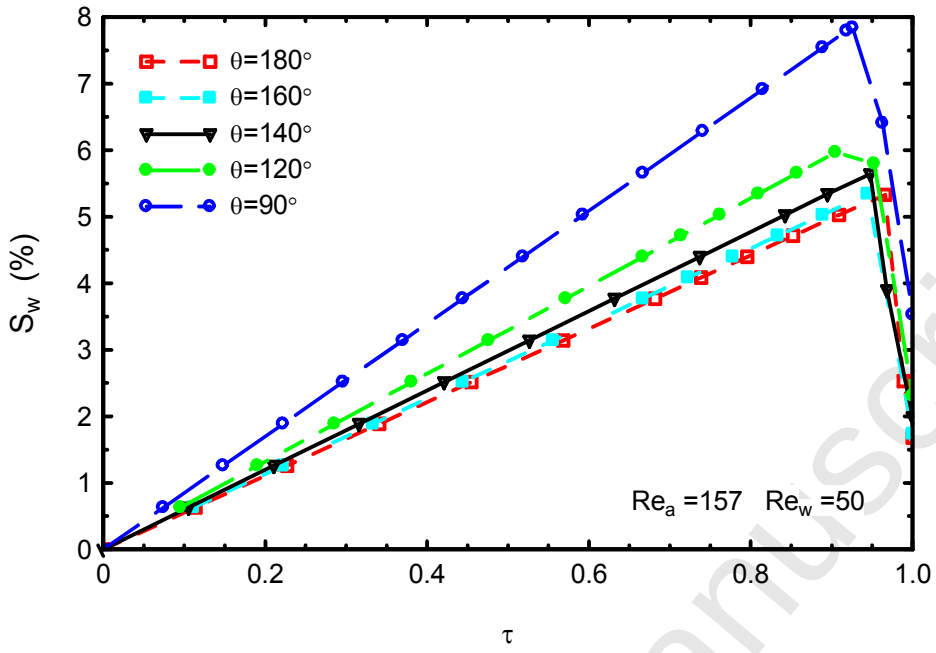

Figure 9 Effect of static contact angle on the water volume saturation in the microchannel

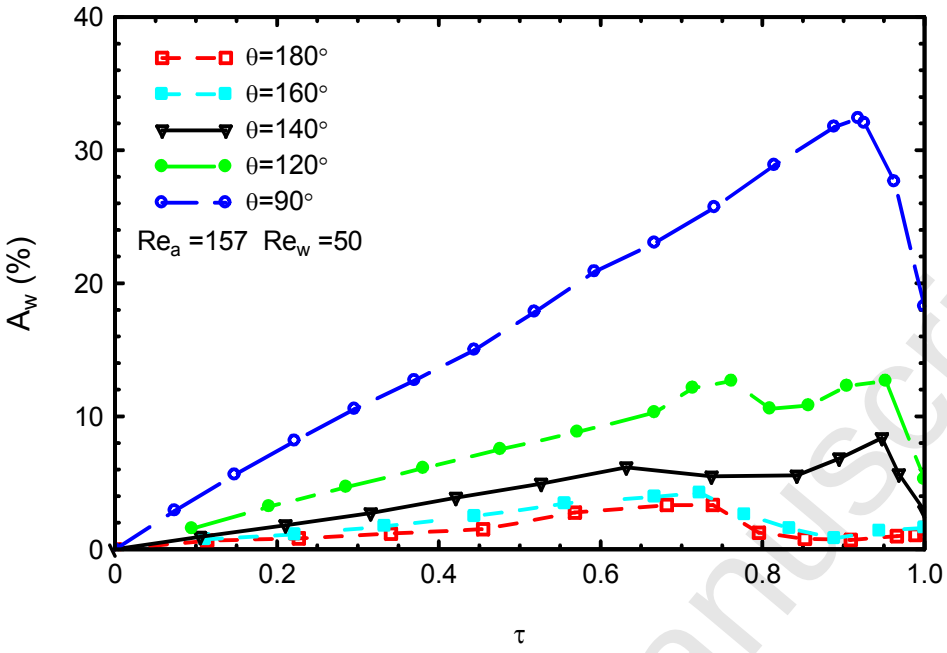

Figure 10 Effect of static contact angle on the water coverage ratio

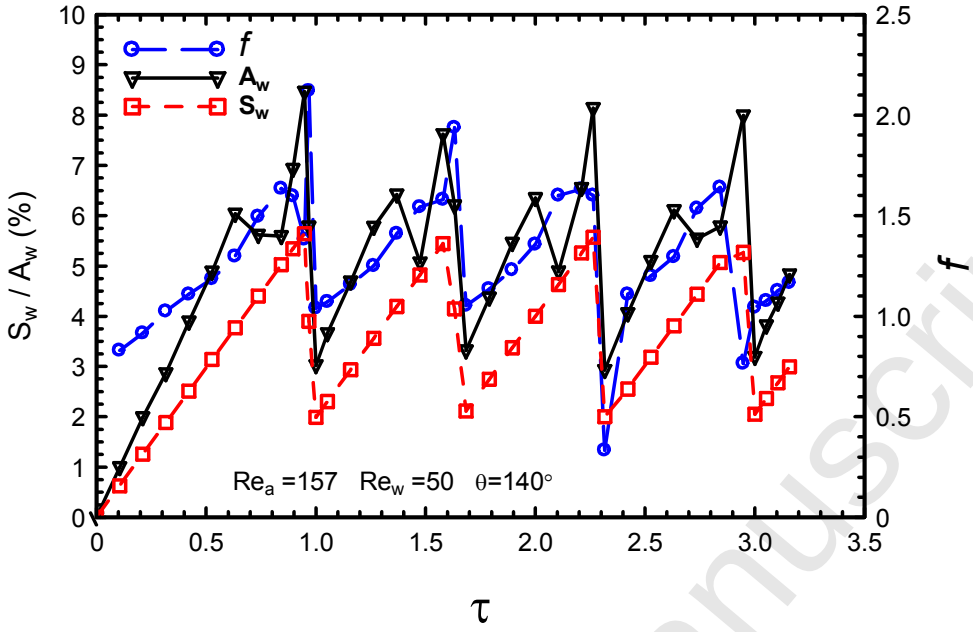

Figure 11 Periodic variations of the flow resistance coefficient, water volume saturation and water coverage ratio for the baseline case

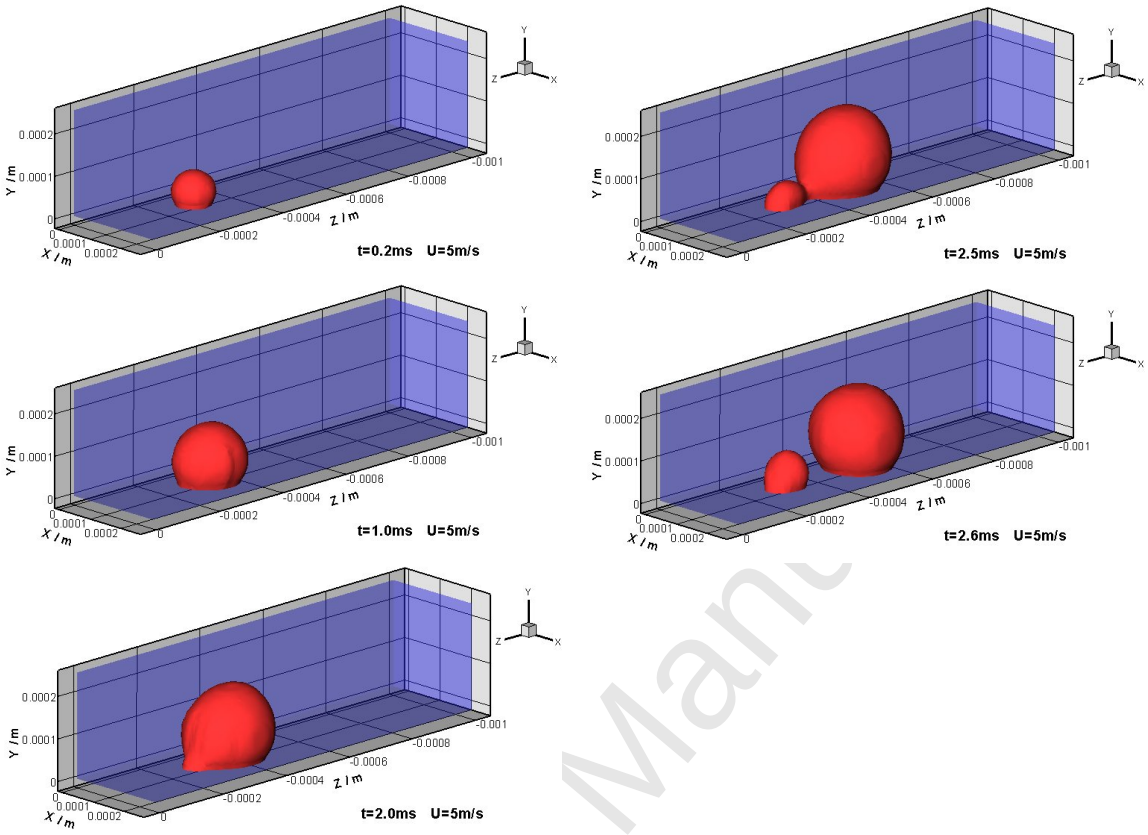

Figure 12 Time evolution of the emerging water droplet into a microchannel with the air inlet velocity of 5 m/s (Re_a=79)

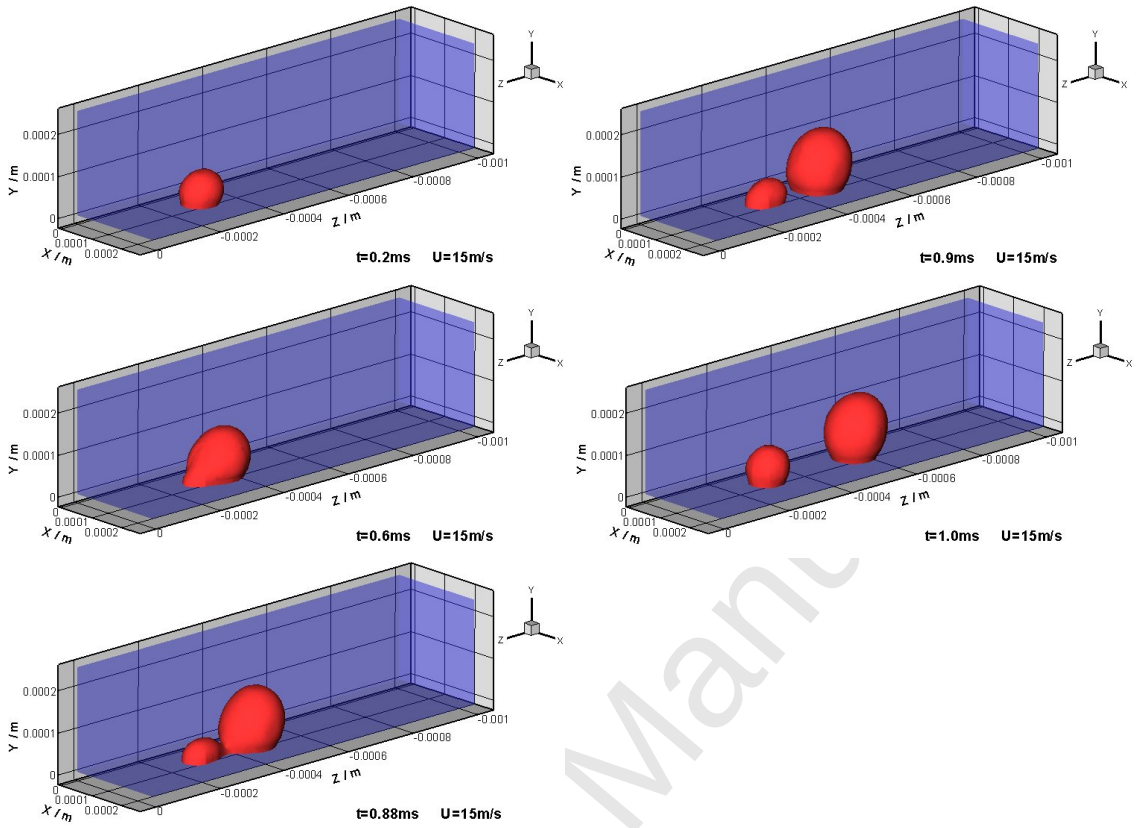

Figure 13 Time evolution of the emerging water droplet into a microchannel with the air inlet velocity of 15 m/s (Re_a=236)

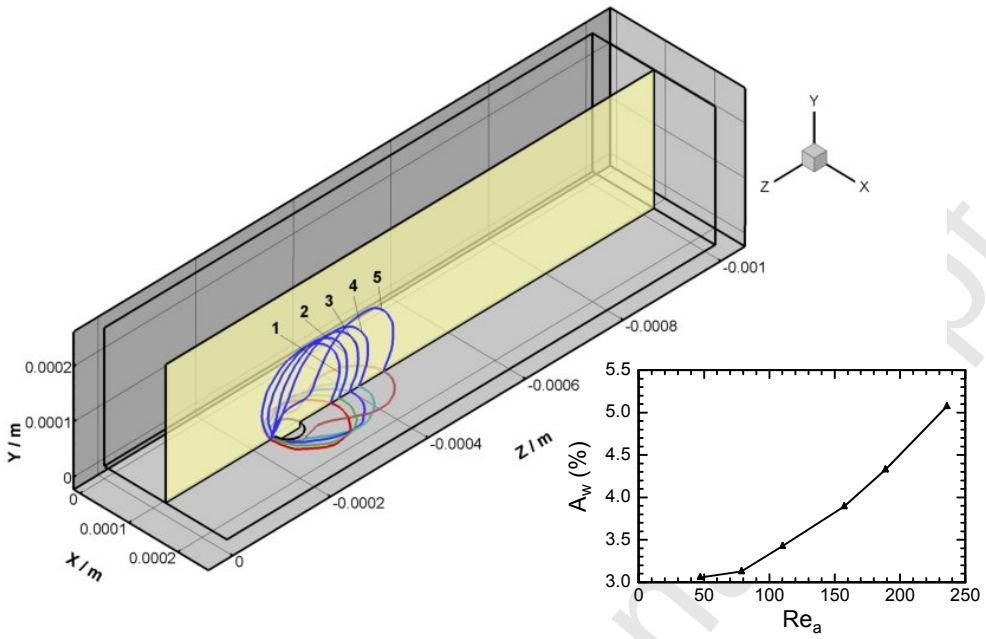

Figure 14 Three phase contact lines and coverage ration for equivalent water volume at different air inlet velocity: 1-U=3m/s (Re_a=47), 2-U=5m/s (Re_a=79), 3-U=10m/s (Re_a=157), 4-U=12m/s (Re_a=189), 5-U=15m/s (Re_a=236)

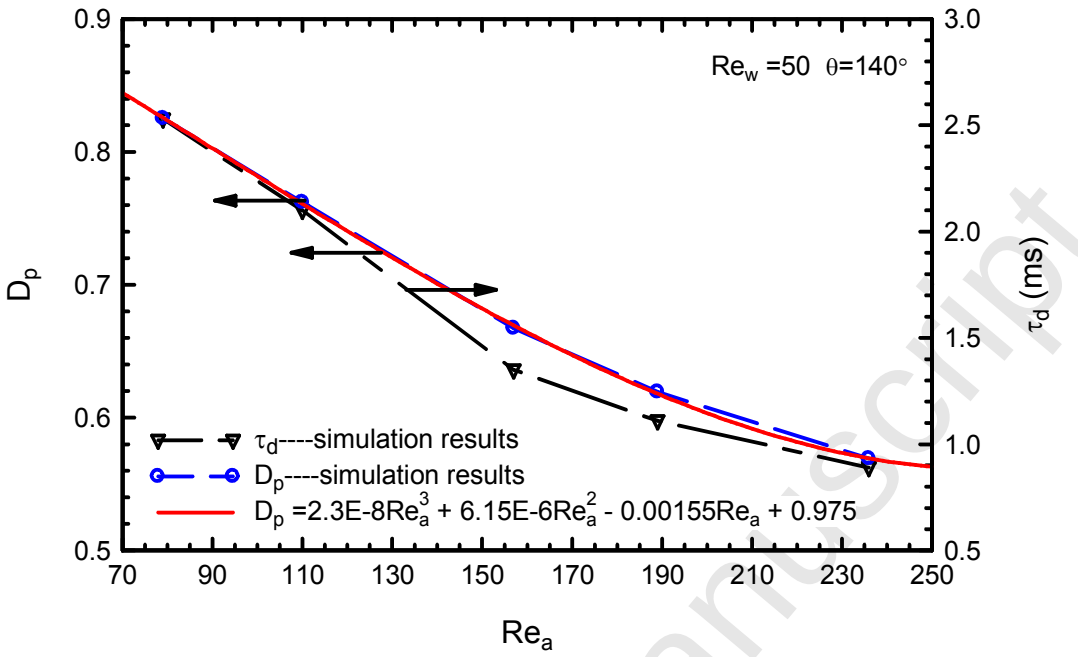

Figure 15 Detachment diameter of the water droplet varies with the Reynolds number of air flow

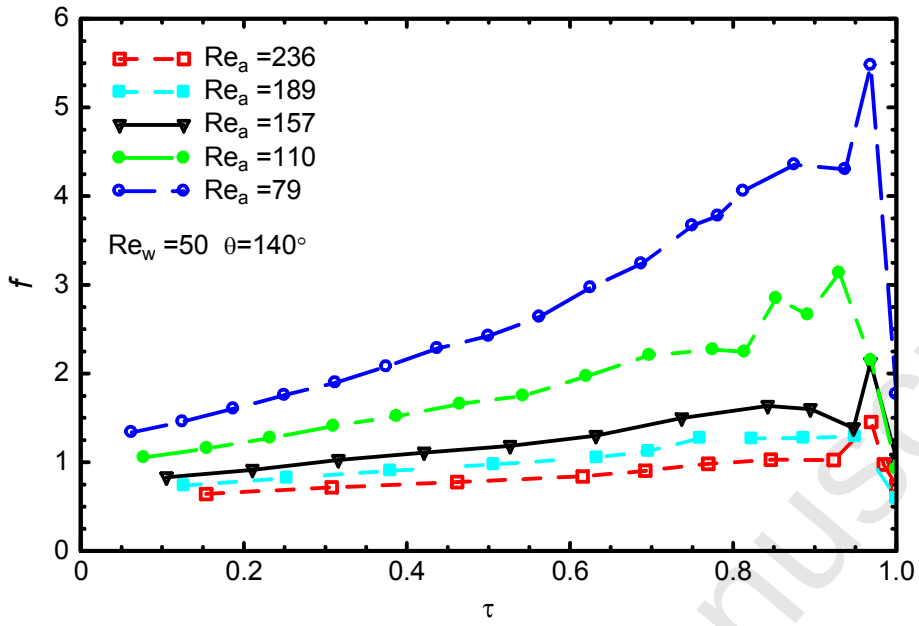

Figure 16 Effect of the Reynolds number of air flow on the flow resistance coefficient

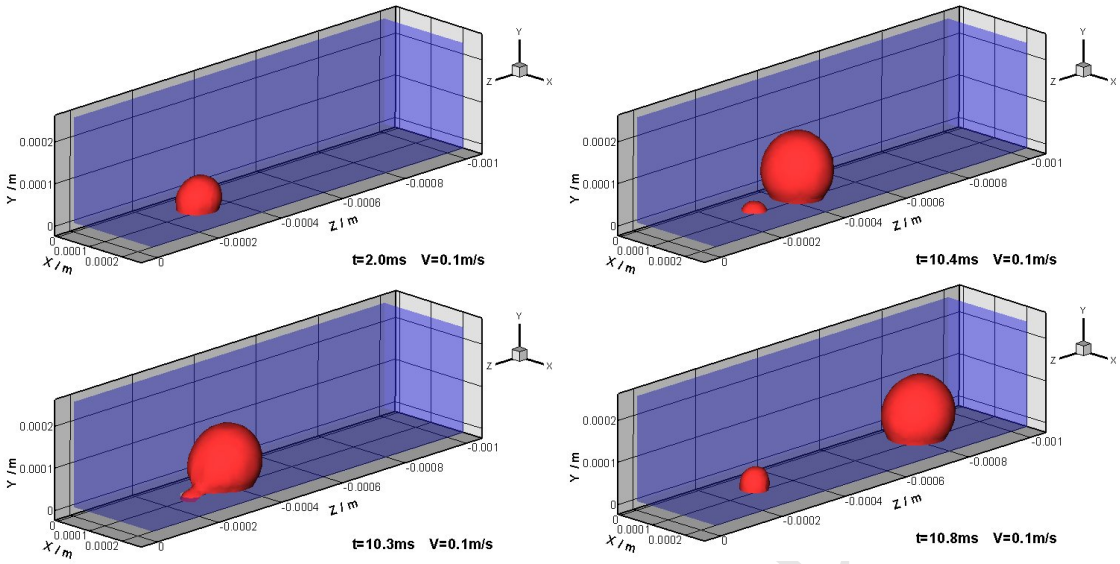

Figure 17 Time evolution of the emerging water droplet into a microchannel with the water injection velocity of 0.1 m/s (Re_w=5)

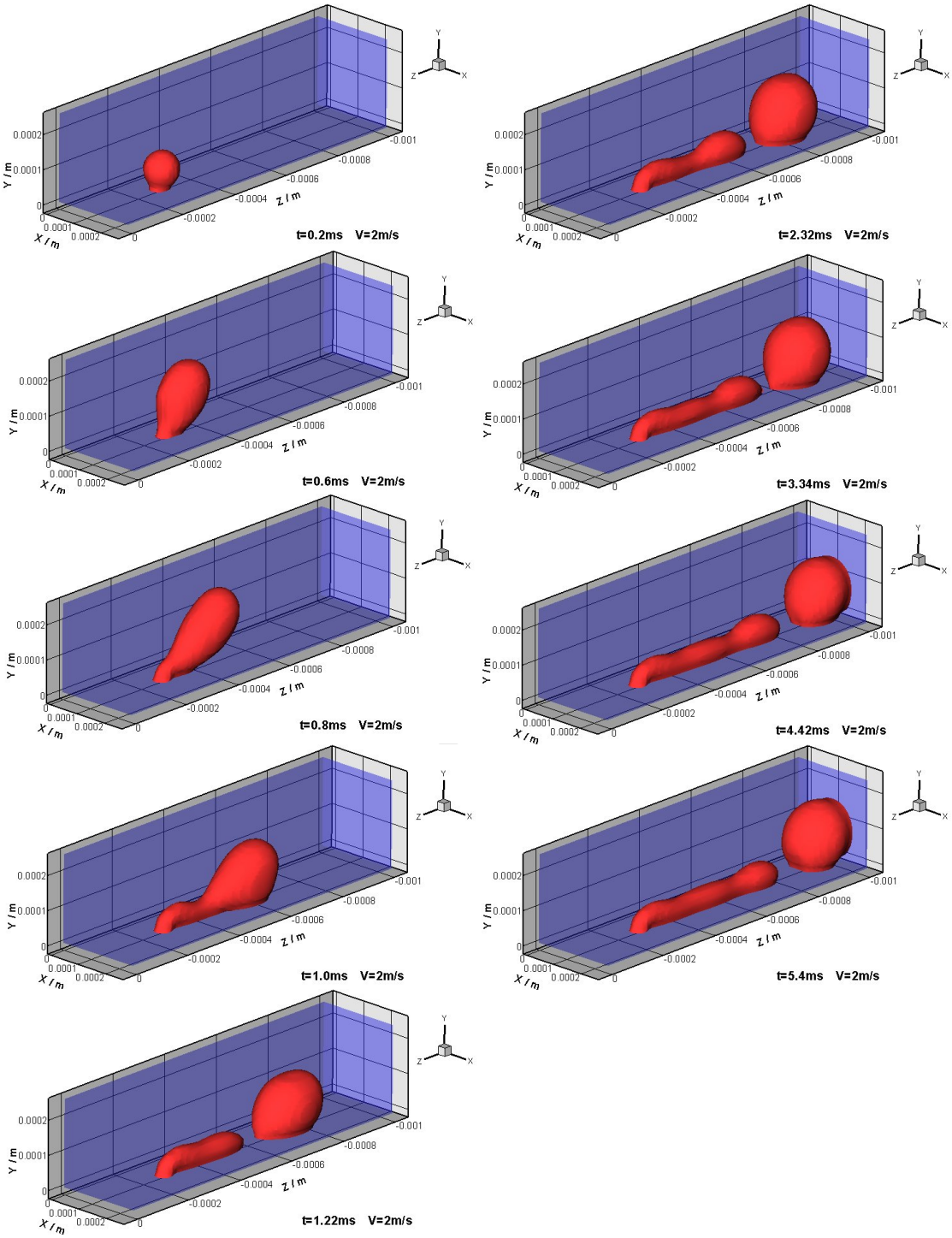

Figure 18 Time evolution of the emerging water droplet into a microchannel with the water injection velocity of 2 m/s (Re_w=100)

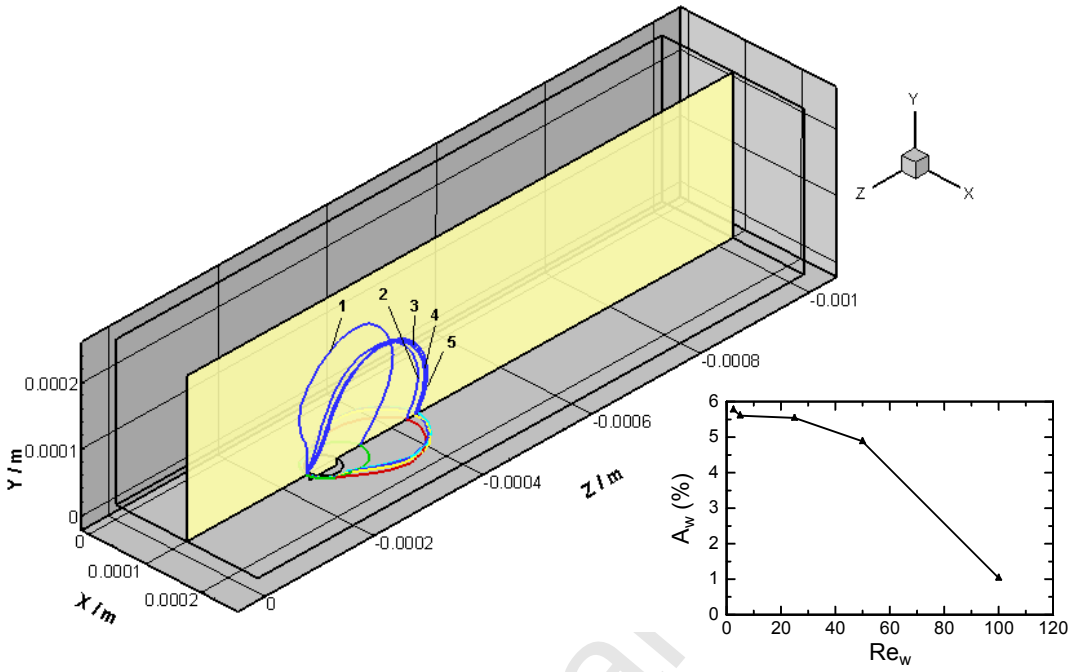

Figure 19 Three phase contact lines and coverage ratio for equivalent water volume at different water injection velocity: 1-V=2m/s (Re_w=100), 2-V=1m/s (Re_w=50), 3-V=0.5m/s (Re_w=25), 4-V=0.1m/s (Re_w=5), 5-V=0.05m/s (Re_w=2.5)

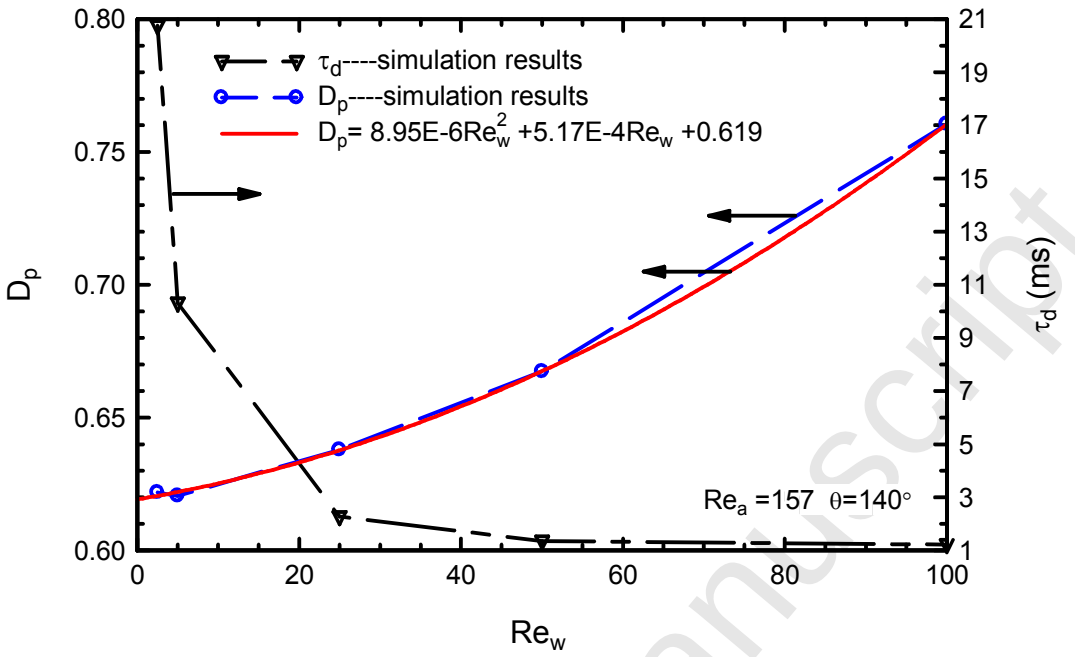

Figure 20 Detachment diameter of the water droplet as a function of Reynolds number of water flow

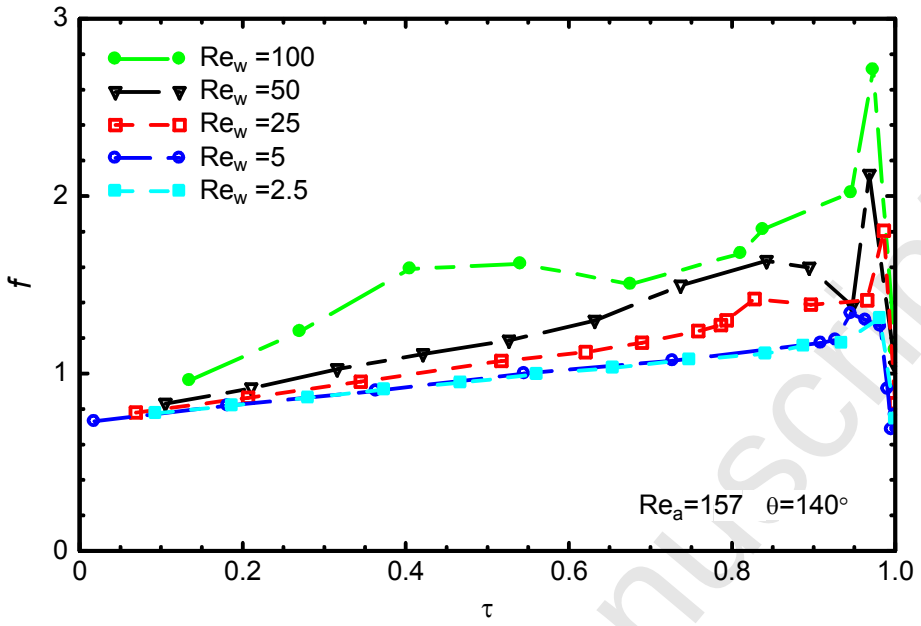

Figure 21 Effect of the Reynolds number of water flow on the flow resistance coefficient

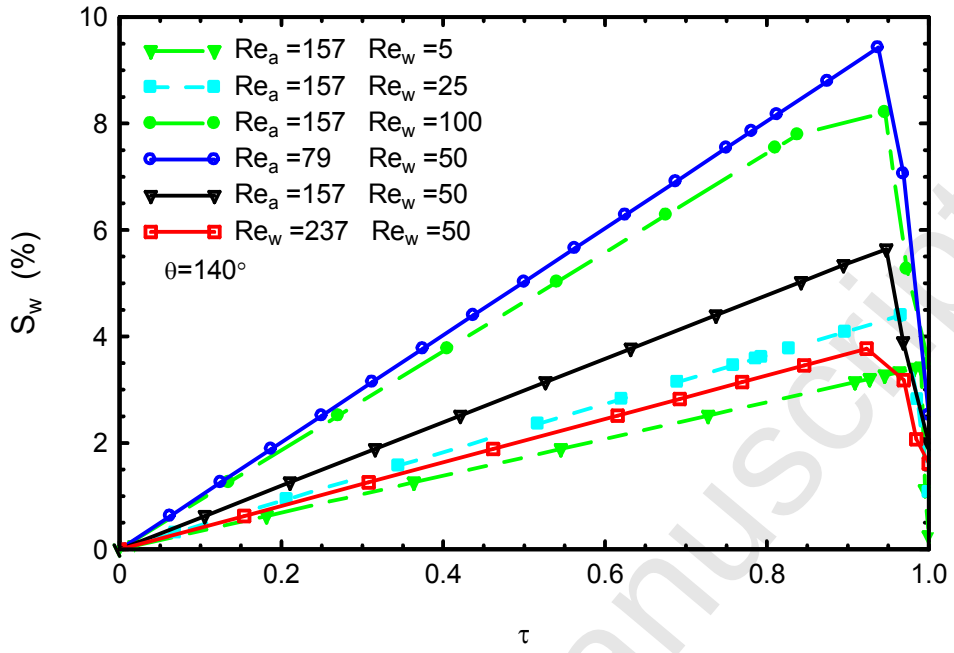

Figure 22 Water volume saturation in the gas channel at different Reynolds number of air and water flow

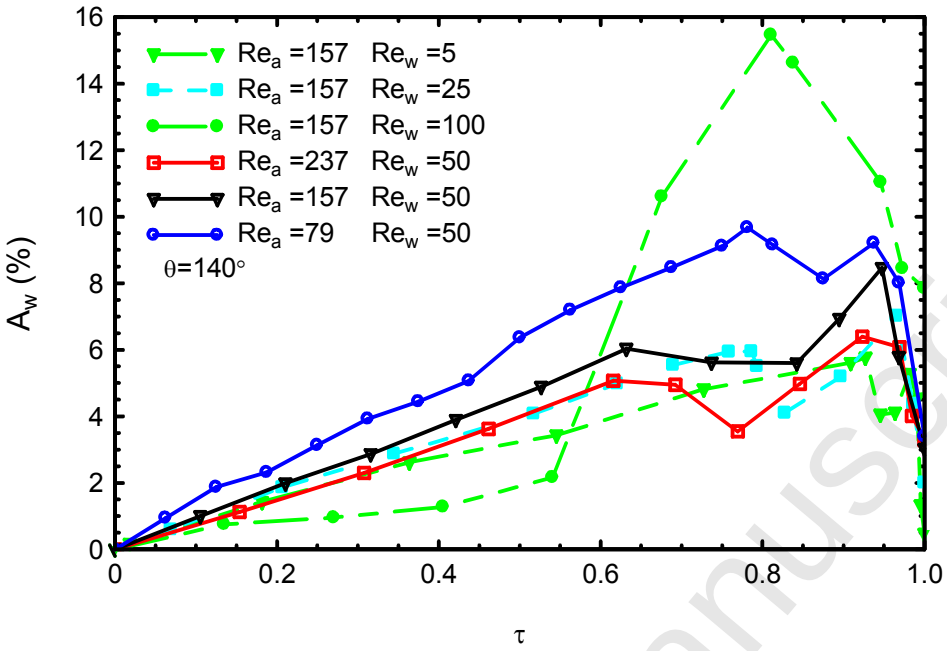

Figure 23 Water coverage ratio at different Reynolds number of air and water flow

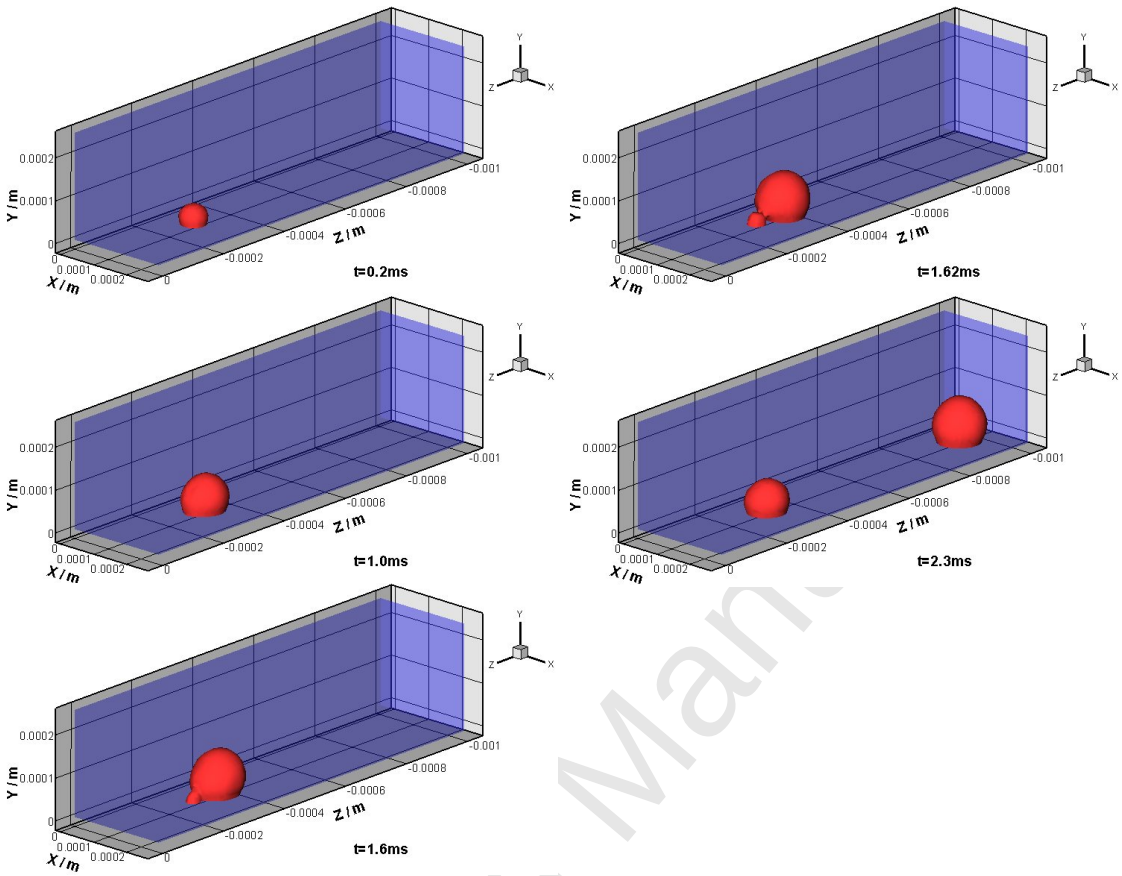

Figure 24 Time evolution of the emerging water droplet into a gas channel with a pore of D=ϕ25 μm

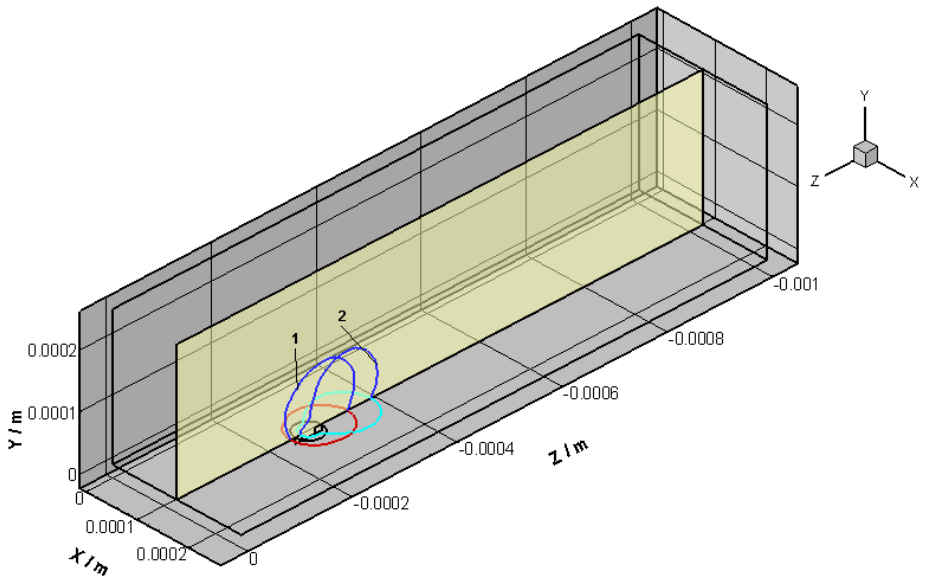

Figure 25 Three phase contact lines for equivalent water volume at different pore size: 1: D=ϕ50μm, 2: D=ϕ25μm